Tollan et al. Progress in Earth and Planetary Science (2017) 4:14
DOI 10.1186/s40645-017-0128-7

Progress in Earth and Planetary Science

RESEARCH ARTICLE Open Access

The responses of the four main substitution mechanisms of H in olivine to H_2O activity at 1050 °C and 3 GPa

Peter M. E. Tollan[1,2], Rachel Smith[1], Hugh St.C. O'Neill[1*] and Jörg Hermann[1,2]

Abstract

The water solubility in olivine (C_{H_2O}) has been investigated at 1050 °C and 3 GPa as a function of water activity (a_{H_2O}) at subsolidus conditions in the piston-cylinder apparatus, with a_{H_2O} varied using H_2O–NaCl fluids. Four sets of experiments were conducted to constrain the effect of a_{H_2O} on the four main substitution mechanisms. The experiments were designed to grow olivine in situ and thus achieve global equilibrium (G-type), as opposed to hydroxylating olivine with a pre-existing point-defect structure and impurity content (M-type). Olivine grains from the experiments were analysed with polarised and unpolarised FTIR spectroscopy, and where necessary, the spectra have been deconvoluted to quantify the contribution of each substitution mechanism. Olivine buffered with magnesiowüstite produced absorbance bands at high wavenumbers ranging from 3566 to 3612 cm^{-1}. About 50% of the total absorbance was found parallel to the *a*-axis, 30% parallel to the *b*-axis and 20% parallel to the *c*-axis. The total absorbance and hence water concentration in olivine follows the relationship of $C_{H_2O} \propto a_{H_2O}{}^2$, indicating that the investigated defect must involve four H atoms substituting for one Si atom (labelled as [Si]). Forsterite buffered with enstatite produced an absorbance band exclusively aligned parallel the *c*-axis at 3160 cm^{-1}. The band position, polarisation and observed $C_{H_2O} \propto a_{H_2O}$ are consistent with two H substituting for one Mg (labelled as [Mg]). Ti-doped, enstatite-buffered olivine displays absorption bands, and polarisation typical of Ti-clinohumite point defects where two H on the Si-site are charge-balanced by one Ti on a Mg-site (labelled as [Ti]). This is further supported by $C_{H_2O} \propto a_{H_2O}$ and a 1:1 relationship of molar H_2O and TiO_2 in these experiments. Sc-doped, enstatite-buffered experiments display a main absorption band at 3355 cm^{-1} with $C_{H_2O} \propto a_{H_2O}{}^{0.5}$ and a positive correlation of Sc and H, indicating the coupled substitution of a trivalent cation plus a H for two Mg (labelled as [triv]). Our data demonstrate that extreme care has to be taken when inferences from experiments conducted at $a_{H_2O} = 1$ are applied to the mantle, where in most cases, a low a_{H_2O} persists. In particular, the higher exponent of the [Si] substitution mechanism means that the contribution of this hydrous defect to total water content will decrease more rapidly with decreasing a_{H_2O} than the contributions of the other substitution mechanisms. The experiments confirm previous results that the [Mg] mechanism holds an almost negligible amount of water under nearly all T-P-fO_2-fH_2O conditions that may be anticipated in nature. However, the small amounts of H_2O we find in substituting by this mechanism are similar in the experiments on forsterite doped with either Sc or Ti to those in the undoped forsterite at equivalent a_{H_2O} (all buffered by enstatite), confirming the assumption that, thermodynamically, C_{H_2O} substituting by each mechanism does not depend on the water concentration that substitutes by other mechanisms.

Keywords: Olivine, Nominally anhydrous minerals, Substitution mechanism, Point defect, Water in the mantle

* Correspondence: hugh.oneill@anu.edu.au
[1]Research School of Earth Sciences, The Australian National University, Building 142, Mills Road, Canberra, ACT 2601, Australia
Full list of author information is available at the end of the article

Introduction

Trace concentrations of hydrogen-bearing point defects can change the mechanical properties of olivine and the dominant phase of the Earth's upper mantle, producing a profound effect on mantle rheology (Demouchy et al. 2007; Karato et al. 1986; Mei and Kohlstedt 2000). Such defects also influence transport properties like electrical conductivity (Karato and Wang 2013). Fourier transform infrared spectroscopy (FTIR) shows that the H substitutes by bonding to O^{2-} anions, producing OH^- species according to the generalised reaction $O^{2-} + H_2O = 2OH^-$. The H incorporation thus depends on the fugacity of H_2O, justifying its colloquial designation as "water". Experimental studies on synthetic systems have identified four principal substitution mechanisms, which can be identified from their different O–H stretching modes, using FTIR spectroscopy. Following Kovacs et al. (2010), we use [Si] to denote the substitution mechanism whereby H is charge-balanced by silicon vacancies, [Mg] for H charge-balanced by Mg vacancies, [triv] for H co-substituting with a trivalent cation, and [Ti] for H co-substituting with titanium. The thermodynamic equilibria describing these four substitutions are:

$$[\mathrm{Si}]: 2H_2O + Mg_2SiO_4 = Mg_2H_4O_4 + SiO_2 \quad (1)$$

$$[\mathrm{Mg}]: H_2O + 0.5\,Mg_2SiO_4 + 0.5\,SiO_2 = MgH_2SiO_4 \quad (2)$$

$$[\mathrm{triv}]: 0.5\,H_2O + SiO_2 + R^{3+}O_{1.5} = R^{3+}HSiO_4 \quad (3)$$

$$[\mathrm{Ti}]: H_2O + 0.5\,Mg_2SiO_4 + TiO_2 = MgTiH_2O_4 + 0.5\,SiO_2 \quad (4)$$

which give the following equilibrium constants for pure forsterite (that is, in the approximation that $a^{ol}_{Mg_2SiO_4}$ is unity):

$$K^{[\mathrm{Si}]} = a^{ol}_{Mg_2H_4O_4} a_{SiO_2} (f(H_2O))^{-2} \quad (5)$$

$$K^{[\mathrm{Mg}]} = a^{ol}_{MgH_2SiO_4} (a_{SiO_2})^{-0.5} (f(H_2O))^{-1} \quad (6)$$

$$K^{[\mathrm{triv}]} = a^{ol}_{R^{3+}HSiO_4} (a_{SiO_2})^{-1} (a_{R^{3+}O_{1.5}})^{-1} (f(H_2O))^{-0.5} \quad (7)$$

$$K^{[\mathrm{Ti}]} = a^{ol}_{MgTiH_2O_4} (a_{SiO_2})^{0.5} (a_{TiO_2})^{-1} (f(H_2O))^{-1} \quad (8)$$

The four substitution mechanisms therefore depend on the activity of silica (a_{SiO2}) in different ways, and in the case of the [triv] and [Ti] substitutions, the chemical potentials (effectively, the availability) of the relevant enabling components, $R^{3+}O_{1.5}$ and TiO_2, respectively. But the most significant implication is that the way that H is incorporated in olivine may vary with the fugacity of H_2O, depending on whether the H atoms needed to achieve charge balance are completely associated with the point defect by being bonded to the oxygen atoms surrounding it in specific locations, or are disordered over the lattice by being bonded to oxygen atoms without regard to location. For example, if the four H atoms of the [Si] mechanism are bonded to oxygen atoms surrounding the Si site vacancy to produce local charge balance (that is short-range order), as recently shown by Xue et al. (2017), then the activity of the $Mg_2H_4O_4$ component would be proportional to its mole fraction, such that $C^{[\mathrm{Si}]}_{H_2O} \propto f(H_2O)^2$. Alternatively, if the H atoms were bonded to four oxygen atoms at random positions in the lattice without short-range order, the configurational entropy of the $Mg_2H_4O_4$ component would be correspondingly greater, with its activity being proportional to its mole fraction to the power of four (or five, if the configurational entropy due to the Si vacancy itself is included), such that $C^{[\mathrm{Si}]}_{H_2O} \propto f(H_2O)^4$ or $f(H_2O)^5$. For the [triv] mechanism, there is only the one H atom per formula unit of $R^{3+}HSiO_4$, so if the position where the H bonds to an oxygen is determined by short-range order with respect to where the R^{3+} cation is substituting, the activity of the $R^{3+}HSiO_4$ component will again be proportional to its mole fraction, but with the result that $C^{[\mathrm{triv}]}_{H_2O} \propto f(H_2O)^{0.5}$. The close association of H substituting by the [triv] mechanism with the R^{3+} cation is demonstrated by the correlation of the wavelength of the [triv] infrared absorption with the ionic radius of the R^{3+} cation (Berry et al. 2007a). If local charge balance proves to be the case, then even at one specific temperature and pressure, the way that "water" is incorporated into olivine should change with the activity of H_2O, a_{H_2O}, defined as $f(H_2O)/f(H_2O)^\circ$, where $f(H_2O)^\circ$ is the fugacity of pure H_2O at the T and P of interest. This is an important consideration when laboratory observations are to be extrapolated to olivine in natural environments such as the Earth's mantle. In the laboratory, experiments are typically conducted at high a_{H_2O} to maximise H_2O contents, which facilitates measurements, but in the Earth's mantle, a_{H_2O} is lowered by the presence of other components, and an upper limit to a_{H_2O} at a given T, P and composition is imposed by partial melting (Green et al. 2010). Whenever amphibole is present, a_{H_2O} is constrained by amphibole-pyroxene-olivine equilibria and is considerably lower than if a free aqueous fluid phase were present (Lamb and Popp 2009).

The aim of the experimental study presented here is to test the relationships between C_{H_2O} and a_{H_2O} for the four principal substitution mechanisms. We chose a representative condition of 3.0 GPa and 1050 °C for experimental convenience, with a_{H_2O} varied using H_2O–NaCl

mixtures. Although the [triv] substitution in natural olivines is likely mostly due to Cr^{3+} and Fe^{3+} (e.g. Tollan et al. 2015), both these elements also occur in olivine in a 2+ valence state, Fe predominantly so, making the determination of the amounts of Fe^{3+} or Cr^{3+} from analysed Fe or Cr impractical. Yet, to understand the [triv] substitution mechanism, it is desirable to know the concentration of the R^{3+} cation in octahedral coordination. For this reason, we sought a redox-insensitive element with a substantial solubility in forsterite, and a large enough ionic radius to substitute into its octahedral sites only—unlike Al, which may also be important in promoting water solubility in olivine (Grant et al. 2007a). There is really only one choice, Sc^{3+}.

Methods/Experimental

Preparation of starting materials

For experiments investigating [Ti], [triv] and [Mg] hydrous defects, powdered synthetic Ti- and Sc-doped forsterite was prepared by a process of solution-gelation. Magnesium nitrate was dissolved in water slightly acidified by nitric acid, with Ti and Sc added to produce forsterite containing 2000 ppm of Ti and Sc, respectively, using ammonium bis(oxalato)oxotitanate(IV) hydrate or scandium oxide. Concentrations in this paper are given in ppm by weight, i.e., $\mu g\ g^{-1}$. Tetra-ethyl orthosilicate was added with ethanol, after which a few drops of ammonia initiated the gelation process, with the mixture then left overnight to allow complete precipitation. The precipitate was dehydrated by heating on a hot plate at low temperatures for 24 h followed by intensive heating, first over a Bunsen burner and then in a box furnace at 600 °C. Pure forsterite, produced by the same method (but without the addition of Sc and Ti), was then mixed with the Sc- and Ti-doped forsterite powders in various ratios to produce the starting compositions for the hydration experiments. Concentrations of Sc and Ti in recovered olivine crystals are given in Table 1. In order to buffer the silica activity, enstatite powder was also produced by sintering synthetic forsterite with SiO_2 in the appropriate stoichiometric proportions. For experiments investigating the [Si] defect, powdered San Carlos olivine was run with synthetic magnesiowüstite ($Fe_{0.7}Mg_{0.3}O$) to produce a low a_{SiO2}, which enhances water substitution by this mechanism.

Table 1 Initial compositions of the H_2O-NaCl fluids and dopant concentrations of recovered forsterite measured by LA-ICP-MS

Experiment	X_{H2O}	Ti or Sc (ppm)	Sd[a] (ppm)
[Si]–San Carlos olivine buffered by magnesiowüstite, Re/ReO_2 fO_2 buffer			
21	0.38	–	–
20	0.44	–	–
32	0.63	–	–
31	0.72	–	–
22	0.81	–	–
30	0.89	–	–
23	1	–	–
[Mg]–undoped forsterite buffered by enstatite, no fO_2 buffer			
84	0.56	–	–
85	1	–	–
[triv]–Sc forsterite buffered by enstatite, no fO_2 buffer			
36	1	586	61
81	1	317	18
82	1	179	11
83	1	950	108
89	0.82	1114	39
91	0.68	1159	8
40	0.50	1228	88
41	0.36	1031	35
75	0.24	1127	16
[Ti]–Ti forsterite buffered by enstatite, no fO_2 buffer			
62	1	307	17
34	1	253	11
37	1	176	19
79	1	88	6
42	1	330	47
76	0.81	292	15
69	0.7	252	23
70	0.57	197	16
77	0.41	164	26
80	0.22	162	24

[a]Standard deviation

Piston-cylinder experiments

One challenge of the experiments was to produce crystals of H_2O-bearing forsterite or olivine large enough for FTIR spectroscopy, but at sufficiently low temperature to avoid melting and excessive dissolution of silica in the fluid, which informed the choice of 1050 °C at 3 GPa. The crystals were grown from the starting materials in a piston-cylinder apparatus. Powders of pure or doped forsterite were packed inside Pt capsules, with a layer of enstatite powder to buffer a_{SiO2}, and oxygen fugacity was controlled by the intrinsic conditions of the assembly (estimated to be approximately equivalent to the fayalite-magnetite-quartz buffer); at which conditions, the only redox-sensitive element, Ti, should be essentially all Ti^{4+} (Mallmann and O'Neill 2009). The experiments using San Carlos olivine and magnesiowüstite were loaded into Au capsules, with oxygen fugacity internally buffered using layers of Re and ReO_2 powders (Pownceby and O'Neill 2000) to ensure a constant Fe^2

$^{+}/Fe^{3+}$ in the olivine and magnesiowüstite. In all experiments, a_{H_2O} was controlled by adding variable amounts of NaCl powder and distilled H_2O. Water was added with a microsyringe, and the amount added was monitored with a microbalance before and after welding to check for evaporative loss. The capsules were contained in MgO-graphite-glass-NaCl assemblies and run in an end-loaded Boyd-type piston-cylinder apparatus. Experiments were performed at 3.0 GPa and 1050 °C for 168 h with temperature monitored by a type B ($Pt_{0.7}Rh_{0.3}$-$Pt_{0.94}Rh_{0.06}$) thermocouple contained within mullite. The experiment was ended by switching off the power. The capsule was pierced and inspected for the presence of free fluid, which confirmed that fluid had not escaped during the run. The capsule was then cut with a scalpel and peeled open. Relatively large forsterite (or olivine) crystals were recovered by picking under an optical microscope.

All the forsterite crystals that were subsequently analysed grew during the experiments, and the finely ground San Carlos olivine completely recrystallised, which is necessary to achieve the equilibrium point-defect structure (Matveev et al. 2001). That all the crystals characterised in this study grew during their synthesis in equilibrium with the buffering assemblages and fluid phase is in contrast to the experimental approach that hydroxylates pre-existing crystals (e.g. Bai and Kohlstedt 1993; Zhao et al. 2004; Gaetani et al. 2014). In this latter approach, H moves into the crystal by solid-state diffusion, but the pre-existing point-defect structure of the olivine crystal is conserved. This phenomenon was exploited by Bai and Kohlstedt (1993) to study olivine pre-equilibrated at different oxygen fugacities at atmospheric pressure and then hydroxylated at one oxygen fugacity at a given temperature and pressure. In such experiments, the point-defect structure under which the water is incorporated is metastable and distinguishable to that expected at global equilibrium (Matveev et al. 2001). A spectacular example of conserving pre-existing point-defect structure is the study of Jollands et al. (2016) on the decoration of Ti^{3+} in forsterite to form the [triv] substitution, by hydroxylation under oxidizing conditions. Stabilizing Ti^{3+} in forsterite requires highly reducing conditions (Mallmann and O'Neill 2009); accordingly, Jollands et al. (2016) prepared their material using a CO–CO_2 gas mixture with 97% CO at 1500 °C and 1 bar. The hydroxylation was then carried out at oxygen fugacities up to twelve orders of magnitude higher, imposed by the Re–ReO_2 and Ag–Ag_2O buffers at 850 °C and 1.5 GPa (Jollands et al. 2016).

There is unnecessary controversy in the literature on the interpretation of experimental results on the incorporation of water in olivine due to the failure to distinguish clearly between the two types of experiments, those aimed at achieving global equilibrium under the conditions at which the water is incorporated and those aimed at hydroxylating existing point-defect structures and compositions, including the minor-element concentrations that determine the amounts of water associated with the [triv] substitution mechanisms. We suggest that to reduce the confusion, all experiments should be labelled "G-type" if global equilibrium is the target and "M-type" if a metastable equilibrium is sought. The experiments reported here are G-type. The interpretation of M-type experiments is likely to be the more difficult by far, because the metastable substitutions depend on the rates of diffusion of the point-defects and/or elements that enable them; in contrast, the global equilibrium that is the aim of a G-type experiment is independent of transport phenomena, by definition. The interpretation of M-type experiments may therefore be aided by H diffusion studies (e.g. Mackwell and Kohlstedt 1990; Demouchy and Mackwell 2006; Padron-Navarta et al. 2014). One potential problem is if the experimental products fall in the no man's land between the two types.

Fourier transform infrared spectroscopy

The forsterite and olivine crystals were analysed by FTIR spectroscopy, using a Bruker Tensor 27 infrared spectrometer with a liquid nitrogen-cooled mercury cadmium telluride detector coupled to a Bruker Hyperion infrared microscope. The analysis chamber was continuously purged with dry air in order to minimise interference of the intrinsic forsterite absorbance band by atmospheric background. Individual crystals were placed on a 100 μm Cu wire grid and measured in transmission mode with polarised and unpolarised light. For polarised measurements, crystal orientation was deduced through comparison of the silicate overtone region (~1200–2200 cm^{-1}) with reference spectra for each principal orientation (Lemaire et al. 2004). Background analyses were taken at regular intervals, and both sample and background measurements were the average of 64 individual scans at a resolution of 4 cm^{-1}. After analysis, the acquired spectra were processed using the Bruker OPUS© software package. Any residual atmospheric contamination was minimised by application of the atmospheric compensation tool, followed by baseline correction using the "concave rubber band" software tool using 64 baseline points and four iterations. Occasionally, a further baseline correction was applied in order to remove broad absorbance bands due to fluid inclusions.

Quantification of data

The areas beneath the major absorbance bands from each experiment were calculated using the integration function of the OPUS software package, and the resulting absorbance

value was normalised to a thickness of 1 cm. Crystal thickness was determined by exploiting the relationship with absorbance in the silica overtone region (1625–2150 cm^{-1}), whereby thickness (in microns) is calculated by dividing the integrated absorbance of the overtones (between 1625 and 2150 cm^{-1}) by the appropriate coefficient. For unpolarised measurements, the coefficient of Shen et al. (2014) was used (0.553). For polarised measurements, coefficients specific for each principal axis were determined by conducting unpolarised and polarised measurements on the same crystal and comparing the respective overtone absorbances. By doing this for multiple crystals, we established coefficients of 0.75, 0.50 and 0.56 for *a*, *b* and *c*-axes, respectively, which were then used in all subsequent thickness calculations for polarised data. Water contents for polarised measurements were calculated by summing the normalised absorbance of each major band along each of the three principal axes and dividing by the integral absorption coefficient. For each experiment design, only the absorbance due to the principal bands is reported (see Table 2 for the integration ranges used), guided by previous experimental and theoretical studies that have reported the association of different defects with specific band positions (e.g., Lemaire et al. 2004; Berry et al. 2005; Walker et al. 2007; Kovacs et al. 2010; Umemoto et al. 2011; Ingrin et al. 2013). Any additional less intense bands at distinctly different wavenumbers were not included in calculations of water, with the exception of bands attributed to Mg vacancies, which are reported separately. The reported uncertainty in the water contents is the standard deviation from measurements of many individual crystals, and is a measure of precision rather than accuracy, as it does not include systematic or semi-systematic uncertainties due to additional factors such as errors in published absorption coefficients, thickness calibrations and baseline corrections, which are likely to be significant, but are difficult to quantify. For the unpolarised absorbances, the measurements from at least 12 crystals from each experiment were averaged, divided by the same integral absorbance coefficient and then multiplied by three, following the method of Kovacs et al. (2008). Uncertainty in water contents following this method is dependent on the degree of polarisation of the defects, the absolute water contents and any unintentional bias in orientation due to crystal shape. Based on this and the comparison with Fig. 1 of Kovacs et al. (2008), an uncertainty of 10% was applied to all unpolarised data.

Spectral deconvolution

When appropriate, complex spectra were deconvoluted in order to isolate the absorbance of individual, overlapping bands. We used a similar method to that of Tollan et al. (2015): bands were fit to a Gaussian function by linear least squares regression, with the optimum half-width for each band held constant between spectra such that only band height was allowed to vary. The starting point for each model was the band positions from Ti-free [Mg] experiments. The positions of any additional bands were deduced through the regression procedure.

LA-ICP-MS

The concentrations of Ti and Sc were determined by laser ablation inductively coupled plasma mass spectrometry (LA-ICP-MS). The laser ablation system consists of a CompexPro 110F ArF excimer laser (193 nm wavelength) with a custom-built two-volume ablation cell for rapid aerosol extraction and washout. The laser was run with a frequency of 5 Hz in energy constant mode, which ensured a stable fluence at the sample surface of 3 to 4 J/cm^2. A focused spot with a diameter of 37 μm was used for sample and standard analyses. The cell was connected to an Agilent 7700x ICP-MS, and ablated material was transported to the ICP-MS in a stream of ultra-high purity He and Ar. Analyses were acquired as a time-resolved signal with 20 s of background followed by 40 s of counts on ablated material. NIST 610 and 612 glasses were used as calibration standards, and Si was used as internal standard.

Results and discussion

Each experiment yielded from three to 15 crystals large enough and sufficiently free of fluid inclusions to obtain quantifiable FTIR data. Polarised spectra from the three principal axes were recovered from each experiment, complemented by unpolarised spectra. Water concentrations calculated from both polarised spectra and unpolarised spectra following the method described by (Kovacs et al. 2008)) are in very good agreement for average water concentrations calculated from each experiment, ranging from 50 to 2500 ppm (Fig. 1), but particularly at lower water concentrations which are within the range typical of natural mantle olivine. This is consistent with the theory of Sambridge et al. (2008), as implemented by Kovacs et al. (2008), and illustrates the viability of using unpolarised data to calculate accurate water concentrations in olivine with a variety of defect populations. The concentration of H_2O associated with each species of hydrous point defect shows a clear relationship with the activity of water of the experiment (Fig. 2). Distinctly different polarised band positions and shapes can be identified from experiments investigating each of the different defect types.

Low SiO_2 activity experiments: [Si]

Olivines from experiments conducted at low silica activity (buffered by magnesiowüstite) are characterised by complex polarised spectra consisting of four major absorbance bands and six further minor absorbance bands (Fig. 3). Bands are moderately to strongly polarised, with very small FWHM (full width at half maximum). Parallel

Table 2 Calculated water concentrations in each of the three principal crystallographic orientations using polarised FTIR data and also total water calculated from unpolarised FTIR data using the method of Kovacs et al. (2008)

		E||a			E||b			E||c			Total			
Experiment	X_{H2O}	H_2O (ppm)	sd	*n*	H_2O (ppm)	sd	*n*	H_2O (ppm)	sd	*n*	H_2O (ppm)	sd	Unpolarised H_2O (ppm)	*n*
[Si] integration range 3650–3420 cm^{-1}														
21	0.379	67	23	11	39	24	7	44	7	6	150	33	163	19
20	0.438	164	51	11	55	21	5	49	30	14	268	55	307	22
32	0.63	418	30	12	241	31	12	139	36	12	798	43	676	21
31	0.717	472	40	17	281	28	14	218	22	11	970	49	918	35
22	0.814	609	101	15	381	147	10	248	81	16	1239	178	1147	26
30	0.892	719	124	13	430	88	15	287	75	13	1436	152	1302	34
23	1	1208	104	10	661	138	8	444	43	7	2314	173	2087	14
[Mg] integration range 3268–3107 cm^{-1}														
84	0.56							16	4	11	16	4		
85	1							24	3	15	24	3		
[triv] integration range 3375–3293 cm^{-1}														
40	1	79	5	3	40	5	6	48	3	7	167	7		
41	1	58	6	6	30	2	3	11	2	3	100	6		
75	1	34	5	6	21	6	3	20	2	7	75	8		
36	1	102	4	7	44	4	12	53	6	10	199	6	193	24
82	0.82	91	3	8	46	3	4	50	2	3	187	4	178	21
81	0.68	80	2	6	40	5	4	44	3	6	164	5	152	22
83	0.5	67	4	10	30	2	6	37	5	7	133	5	136	23
91	0.36	58	4	10	24	3	7	29	3	8	111	5	101	20
89	0.24	42	2	5	15	6	1	22	6	4	79	6	76	10
[Ti] integration range 3586–3495 cm^{-1}														
62	1	84	11	3	15	5	6	38	2	8	138	12	140	21
34	1	91	16	12	13	9	7	35	5	7	139	18	146	31
37	1	50	8	6	10	9	6	26	8	9	86	12	81	20
79	1	31	4	5	7	4	4	15	4	6	54	6	57	14
42	1	88	8	13	14	7	8	39	5	7	140	11	142	23
76	0.81	81	4	5	12	4	7	37	2	7	130	6	128	31
69	0.7	73	7	4	12	3	10	29	4	5	115	8	103	22
70	0.57	57	5	11	9	1	4	20	4	5	86	5	94	21
77	0.41	40	4	5	5	2	5	15	1	3	60	4	61	23
80	0.22	25	4	13	5	2	10	10	3	10	40	4	36	22

Only the principal absorption bands that dominate in each experiment were used, as indicated by the integration ranges. The data from the [triv] experiments have had the contribution from [Si] subtracted, as explained in the text. The expected standard deviation of the unpolarised data is ~10%, as discussed in Kovacs et al. (2008)
sd standard deviation in ppm

to E||a, the strongest bands are centred at 3612 cm^{-1} followed by 3578 cm^{-1}. The band at 3612 cm^{-1} shows strong asymmetry, with a prominent shoulder positioned at 3600 cm^{-1}, whilst the band at 3578 cm^{-1} shows minor asymmetry with a small shoulder positioned at 3550 cm^{-1}. Parallel to E||b, the strongest band is centred at 3550 cm^{-1}, followed by the band at 3578 cm^{-1} which has similar intensity as in the E||a direction. The band at 3612 cm^{-1} is also present, but at a much lower intensity than in the E||a direction. Parallel to E||c, only one major band is present, centred at 3566 cm^{-1}. This single band however is strongly asymmetric, with a double shoulder at 3545 and 3533 cm^{-1}. The band at 3612 cm^{-1} is again present, this time at even lower intensities than along either E||a or E||b. None of the other major bands from E||a or E||b are above the limit of detection.

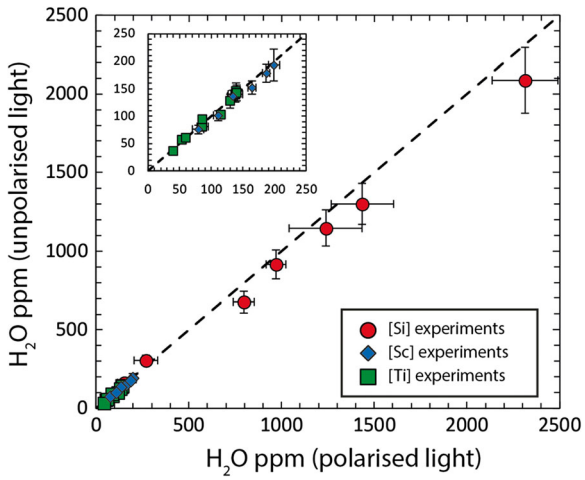

Fig. 1 Comparison of water concentrations for different point defects calculated using polarised light and unpolarised light, following the method of Kovacs et al. (2008). Note that the calculated water contents are based only on the principal absorbance bands from each experiment, as discussed in the "Methods" section. Integration ranges are as follows: [Si] 3650–3422 cm^{-1}; [Ti] 3586–3495 cm^{-1}; [triv] 3375–3293 cm^{-1}

Water associated to titanium: [Ti]

Two series of Ti-doped experiments were conducted: one set at varying a_{H_2O} but fixed bulk Ti concentration and another at fixed a_{H_2O} and varying bulk Ti concentration. Spectra from both types of experiment shared the same absorbance features. Forsterite from experiments doped with Ti reveals less complex spectra than those from [Si] experiments, with only two major bands and one minor band, which are present in each direction (Fig. 4). The two most prominent bands are centred at 3572 and 3525 cm^{-1}, consistent with previous studies (Berry et al. 2005; Kovacs et al. 2010; Padrón-Navarta et al. 2014). The 3572 cm^{-1} band is typically the most intense of the two, by a factor of approximately 2 and 1.5 in the E||a and E||b directions respectively. In the E||c direction, the 3572 cm^{-1} is more intense at high a_{H_2O}, but the ratio of the two peaks decreases to unity as a function of decreasing a_{H_2O}. Due to an overlapping contribution from [Si] bands with the 3572 cm^{-1} band (Padrón-Navarta et al. 2014), spectra from [Ti] experiments were deconvoluted as described in the "Methods" section, and the following discussion of [Ti] data is based on the results of this deconvolution (Fig. 7, Table 4). Titanium-doped forsterite covers a range of Ti contents, from 330 to 88 ppm (Table 1). Multiple

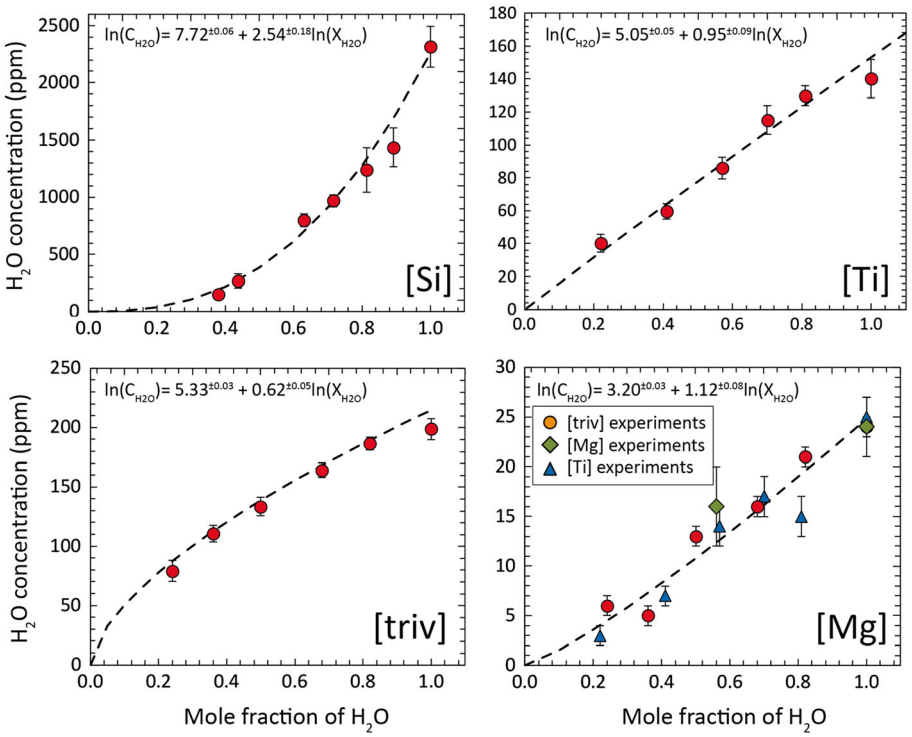

Fig. 2 Variation in water concentration with X_{H2O} in H_2O–NaCl fluids for the four different point defects. The calculated water contents are based only on the principal absorbance bands from each experiment, as discussed in the "Methods" section of the text. The best fit curves are from least squares non-linear regression with weighting of both variables according to the standard deviations in Tables 2 and 3

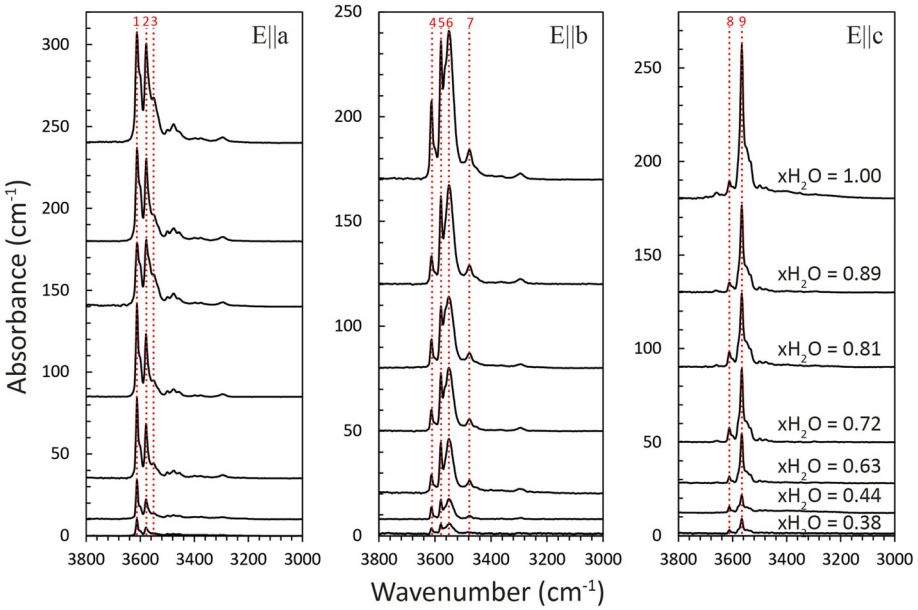

Fig. 3 Polarised spectra measured parallel to principal crystallographic axes for [Si] experiments, ordered from highest water activity (*top*) to lowest (*bottom*). Spectra are the average of multiple measurements, normalised to 1 cm and offset for clarity. The indicated band positions are (1) 3612 cm^{-1}, (2) 3578 cm^{-1}, (3) 3550 cm^{-1}, (4) 3612 cm^{-1}, (5) 3578 cm^{-1}, (6) 3550 cm^{-1}, (7) 3477 cm^{-1}, (8) 3612 cm^{-1} and (9) 3566 cm^{-1}

crystals from the same experiment had similar concentrations, with standard deviations of 5–15%.

Water associated to trivalent cations: [triv]

As with [Ti] experiments, two series were conducted: one with fixed a_{H_2O} and another with fixed Sc concentration, and likewise, spectra from both experiment types were consistent with each other. Scandium-doped forsterite have simple spectra which are consistent with the study of Berry et al. (2007a), with one major band with very small FWHM at 3355 cm^{-1}, which appears strongly in all three directions but most intensely along E||a and a minor band

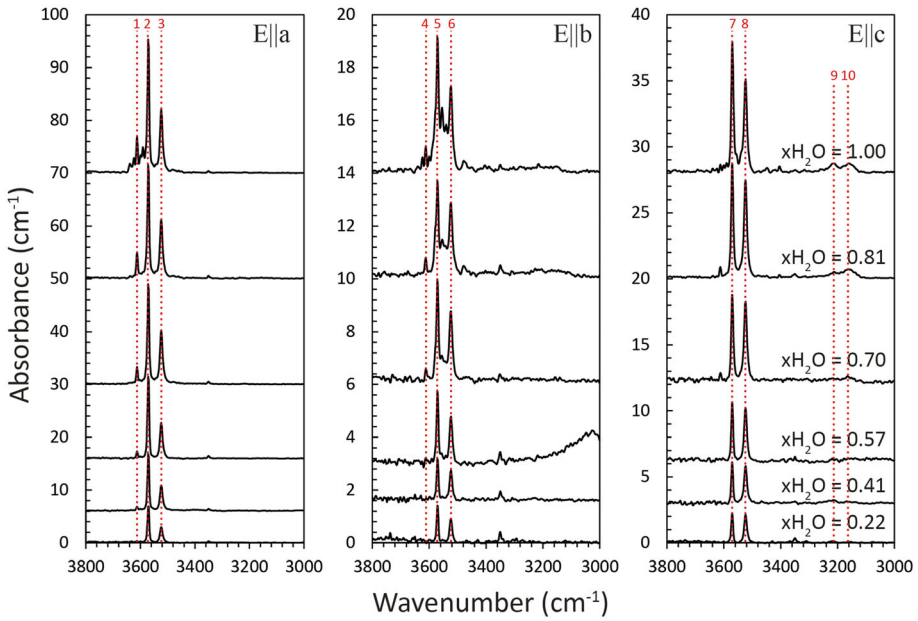

Fig. 4 Polarised spectra measured parallel to principal crystallographic axes for [Ti] experiments, ordered from highest water activity (*top*) to lowest (*bottom*). Spectra are the average of multiple measurements, normalised to 1 cm and offset for clarity. The indicated band positions are: (1) 3612 cm^{-1}, (2) 3572 cm^{-1}, (3) 3525 cm^{-1}, (4) 3612 cm^{-1}, (5) 3572 cm^{-1}, (6) 3525 cm^{-1}, (7) 3572 cm^{-1}, (8) 3525 cm^{-1}, (9) 3220 cm^{-1}, (10) 3160 cm^{-1}

at 3320 cm^{-1}, found principally along E||c (Fig. 5). A further minor, much broader band centred at 3160 cm^{-1} is similar to those found in [Ti] and [Mg] experiments and thus unrelated to the presence of Sc. Average Sc contents of forsterite recovered from the different experiments ranged from 179 to 1228 ppm. Standard deviations are typically less than 10%, but rarely up to 20%.

High SiO_2-activity experiments: [Mg]

Two experiments were run in the system MgO–SiO_2–H_2O with excess enstatite and without Ti or Sc present to create hydrated Mg vacancies, to complement the results from both the [Ti] and [triv] experiments, which were also enstatite-buffered and produced the same absorbance bands in addition to those from the [Ti] and [triv] substitutions (Figs. 4 and 5). The absorption occurs at lower wavenumbers, with two broad bands typically present, one at 3220 cm^{-1} and another at 3160 cm^{-1}, with the former band generally more intense (an exception to this is discussed later). Neither of these bands was produced in [Si] experiments, which were conducted at much lower silica activity. Additional minor bands are observed in the [Mg] experiments, the most prominent of which is centred at 3567 cm^{-1} followed by a number of less intense bands between 3300 and 3500 cm^{-1}.

Band positions and point defect assignments

Olivine and forsterite from [Si], [Ti], [triv] and [Mg] experiments all have distinctive infrared spectra, indicating that the experiments were successful in producing different point defects. This is confirmed by the different polarisations of the principal bands for olivine/forsterite from each type of experiment (Fig. 6), requiring that O–H bonds be configured differently for each defect. Bands for olivine from [Si] experiments show the strongest absorbance along E||a, followed by E||b and E||c. For forsterite from [Ti] experiments, the order of strongest absorbance is E||a, E||c and then E||b, whilst for forsterite from [triv] experiments, E||a shows the strongest absorbance, with E||b and E||c the same within uncertainty. [Mg] bands meanwhile are only present along E||c. We have assigned the bands from each experiment to a different point defect stoichiometry based on the design and intent of each experiment and through comparison with similar experiments/spectra from the literature.

Bands for olivines from [Si] experiments (Fig. 3) have similar or identical positions with those in other low silica activity (wüstite- or magnesiowüstite-buffered) experimental studies (Aubaud et al. 2007; Lemaire et al. 2004; Padrón-Navarta et al. 2014; Withers and Hirschmann 2008), but also occur in experiments buffered at high silica activity conducted at significantly higher pressures (Smyth et al. 2006), with the highest intensity bands located at high wavenumbers (>3500 cm^{-1}). The precise location of the bands is occasionally offset by 1–8 cm^{-1}: for example, the band at 3550 cm^{-1} is found at slightly higher wavenumbers in other studies, likely due to differences in the configuration of Fe in M sites adjacent to the hydrated Si vacancy (Blanchard et al. 2017). The general complexity and number of bands is much

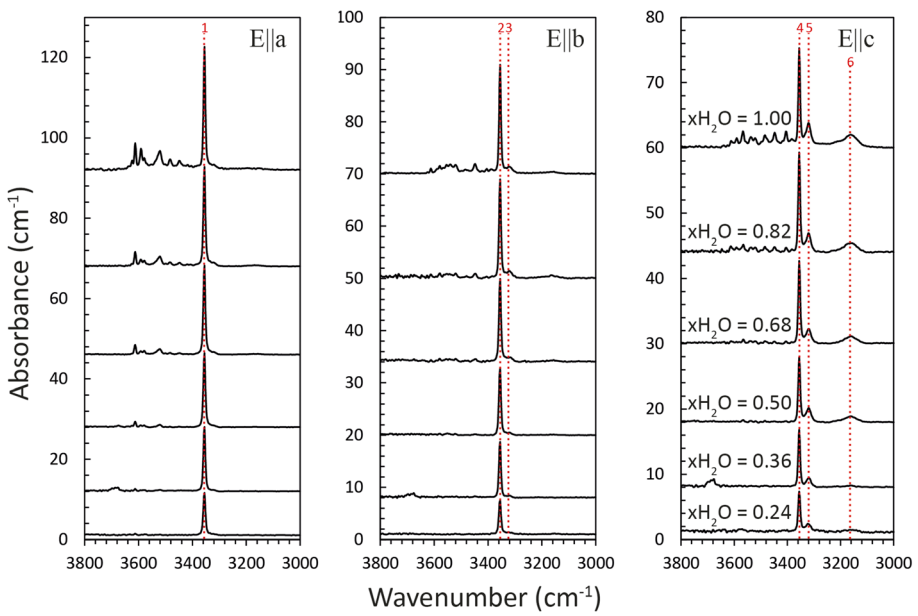

Fig. 5 Polarised spectra measured parallel to principal crystallographic axes for [triv] experiments (Sc-doped), ordered from highest water activity (*top*) to lowest (*bottom*). Spectra are the average of multiple measurements, normalised to 1 cm and offset for clarity. The indicated band positions are (1) 3355 cm^{-1}, (2) 3355 cm^{-1}, (3) 3320 cm^{-1}, (4) 3355 cm^{-1}, (5) 3320 cm^{-1} and (6) 3160 cm^{-1}

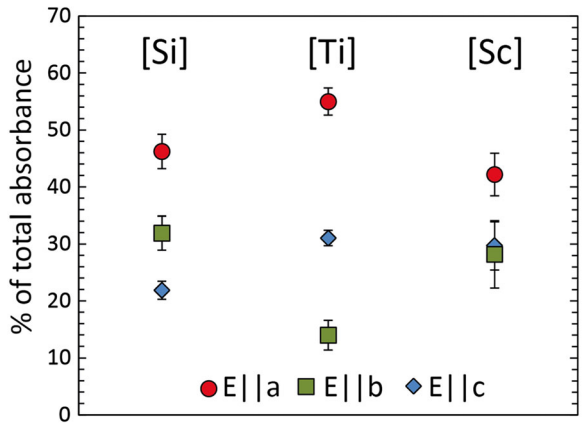

Fig. 6 Percentage that the absorbance from each orientation contributes to the total absorbance, for different point-defect types. The absorbance associated with [Mg] defects is only detectable along E||c

greater for defects in olivine from [Si] experiments than any other defect type investigated, indicating the involvement of multiple hydroxyl groups in a number of configurations, as explored through atomistic simulations (Balan et al. 2011; Umemoto et al. 2011; Walker et al. 2007). These observations are all consistent with hydrogen bonding to oxygen atoms surrounding silicon vacancies in the olivine structure, as denoted in Eq. 1 and supported by other studies investigating hydrous defect configurations (Ingrin et al. 2013; Blanchard et al. 2017).

Forsterite from the [Ti] experiments also displays absorbance at high wavenumbers, with bands at 3572 and 3524 cm^{-1} being the most intense (Fig. 4). These band positions are unique to [Ti] experiments, and are identical in wavenumber to previous experimental studies of Ti-doped olivine/forsterite (Berry et al. 2005; Kovacs et al. 2010; Padrón-Navarta et al. 2014). They are also the most commonly observed bands in natural upper mantle olivines sampled in spinel peridotite xenoliths, although their contribution to the total absorbance for a given sample varies significantly (Berry et al. 2005; Denis et al. 2013; Schmädicke et al. 2013). Precise band positions generally vary slightly in the literature, which can be explained in part due to the overlap with the [Si] bands at 3578–3580 and 3566 cm^{-1} (Padrón-Navarta et al. 2014). As with previous studies using Ti as a dopant, we assign these bands to formation of a titano-clinohumite point defect within the forsterite structure (Eq. 2), with the resultant generation of a silicon vacancy explaining the similar wavenumbers to bands from [Si] experiments.

The [triv] experiments produced forsterite with absorbance dominated by a single intense band at 3355 cm^{-1}, similar to the Sc-doped experiments of Berry et al. (2007a). This band, along with the minor band at 3320 cm^{-1}, are unique to the [triv] experiments and are assigned to coupled substitution of Sc^{3+} and H^{+}, with the latter providing local charge balance in octahedral site vacancies (Eq. 3). In natural olivines, bands in this wavenumber region occur sporadically, but can occasionally be the dominant defect type, particularly in olivines with very low Ti concentrations (Soustelle et al. 2013; Soustelle et al. 2010; Tollan et al. 2015). The precise position, polarisation and relative intensity of bands from natural olivines differ from those produced in our [triv] experiments, indicating that Sc is not a significant partner, as expected from the much lower concentrations of Sc in natural mantle olivine (typically 2–10 ppm). Ferric iron and Cr^{3+} are both much more abundant trivalent cations in natural olivine and are the likely candidates for the 3+ cation partnering H in this substitution mechanism (Tollan et al. 2015; Blanchard et al. 2017).

Two experiments were conducted specifically investigating [Mg] defects, which are generated most strongly under conditions of high silica activity (orthopyroxene/enstatite-buffered). However, identical bands were produced in all the other enstatite-buffered experiments, but not in the [Si] experiments, which were buffered at low a_{SiO_2} by magnesiowüstite. The bands associated to the [Mg] defect are located at lower wavenumbers, and display characteristically broad absorbance with large FWHM, but only along E||c. Two bands can be distinguished, one centred at 3160 cm^{-1} and another at 3220 cm^{-1}. Both of these bands are present in [Ti] and [Mg] experiments, with the band at 3220 cm^{-1} more intense. In [triv] experiments however, the band at 3160 cm^{-1} is more intense. Lemaire et al. (2004), Balan et al. (2011) and Umemoto et al. (2011) suggested that these band positions can be explained by protonation of vacant M1 and M2 sites. However, as pointed out by Blanchard et al. (2017), protonation of the M2 site was never explicitly modelled in these studies, and the variation in band position can be better explained by protonation of an M1 vacancy coupled with Fe^{2+} occupying either a neighbouring M1 or M2 site. Preferential ordering of Sc into one of the two kinds of octahedral sites would imply that vacancies concentrated in the other kind, with the H^{+} bonding to an O^{2-} surrounding the vacancy, to even out the perturbation of charge density. Based on site occupancy arguments in Blanchard et al. (2017), it is perhaps more likely that the greater intensity at 3160 cm^{-1} in [triv] experiments indicates that Sc is partitioning more favourably onto the larger M2 site, with the vacancy and its compensating H favouring M1, assuming that Sc is behaving similarly to Fe^{3+}. Similar or identical bands to these are commonly observed in other experimental studies and also in natural samples (e.g., Aubaud et al. 2007; Férot and Bolfan-Casanova 2012; Gaetani et al. 2014; Grant et al. 2007a, b). Band positions vary much more than bands from other defects, which may be due to the very broad and often low intensity of these bands,

making it difficult to precisely locate the wavenumber of maximum intensity. In addition, partitioning of a wide range of trace and minor cations onto either or both octahedral sites could result in slightly different O–H bond lengths and an associated wavenumber shift.

Although our experimental strategy aims to emphasise only one of the four types of substitution mechanism in each group of experiments, it is important to recognise that absorption bands corresponding to some of the other substitution mechanisms are a minor feature of most of the spectra (Figs. 3, 4 and 5). A small band at 3350 cm^{-1} is often observed in [Si] and [Ti] experiments, most likely due to hydrogen bonding with trace amounts of Fe^{3+} (Berry et al. 2007a). However, the most significant additional band is the presence of relatively strong absorbance associated with silicon vacancies in [Ti] and [triv] experiments, despite the fact that they were run under enstatite-buffered conditions $\left(\text{high } a_{SiO_2}\right)$. Whilst this observation combined with the general decrease in the ratio of water associated with Mg vacancies (i.e. $C_{H_2O}^{[Mg]}$) to that associated with Si vacancies $\left(C_{H_2O}^{[Si]}\right)$ with decreasing total water content (C_{H_2O}) in the [Ti] experiments (Table 3) is qualitatively consistent with the theoretical calculations of Walker et al. (2007), the actual values of this ratio differ from those calculated by Walker et al. (2007), which predicts a greater decrease as total water content increases (see Fig. 3 of Walker et al. (2007)). Nevertheless, the important observation here is that at lower water activities, hydrated Mg vacancies are favoured over hydrated Si vacancies when all other conditions are kept constant, the reasons for which we address next.

Table 3 Calculated water contents in ppm for the [Mg] bands (hydrated Mg vacancies), based on the integration range 3268–3107 cm^{-1}, from [Ti] and [triv] experiments. Also reported is the water associated with silicon vacancies in [Ti] experiments, calculated from band deconvolution. See the text for further details

Experiment	X_{H2O}	[Mg] H_2O (ppm)	sd	[Si] H_2O (ppm)
[Ti]				
62	1			30
34	1			29
37	1			26
79	1			32
42	1	25	2	25
76	0.81	15	2	15
69	0.7	17	2	10
70	0.57	14	2	5
77	0.41	7	1	2
80	0.22	3	1	1
[triv]				
36	1	24	1	
82	0.82	21	1	
81	0.68	16	1	
83	0.5	13	1	
91	0.36	5	1	
89	0.24	6	1	

Relationships with water activity, a_{H_2O}

Significant controversy prevails regarding the issue of relating measured absorptions to water contents. Several theoretical and experimental studies have demonstrated that the absorption coefficient should vary as a function of the vibrational energy characteristic of the configuration of H in a given defect (e.g., Kovacs et al. 2010; Balan et al. 2011; Ingrin et al. 2014; Blanchard et al. 2017). Hence, there should be a negative correlation between the infrared wavenumber and absorption coefficient. At present, however, whilst computational studies are useful in defining the expected trend, absolute values are not reliable. Experimental studies on the other hand produce more accurate values, but have so far explored a relatively small number of appropriate defects. Amongst the available experimental studies, the value of 28,450 L mol^{-1} cm^{-2} from Bell et al. (2003) has been most widely applied. Kovacs et al. (2010) produced an identical value for olivine bearing [Ti] and [triv] defects, although their absorption coefficients for [Si] and [Mg] defects were compromised by the occurrence of a previously unknown defect involving boron which comprised a significant proportion of the water in the "Pakistani" olivine used in their experiments (Ingrin et al. 2014). More notably, Withers et al. (2012) determined a strikingly different value of 45,200 L mol^{-1} cm^{-2} for synthetic olivines with most of the absorbance in their infrared spectra occurring at similarly high wavenumbers to the spectra in the study of Bell et al. (2003), albeit with a different defect ([Si] as oppose to [Ti]). This study utilised elastic recoil detection analysis as the matrix-independent method of absolute H_2O concentration determination, as opposed to nuclear reaction analysis which was used by Bell et al. (2003). The reason for the discrepancy between absorption coefficients is currently unclear, but since the absolute determination of water content is of minor significance for this study, we apply the more commonly used value (Bell et al. 2003), 28,450 L mol^{-1} cm^{-2}, with the caveat that calculated values may be systematically wrong as a result, something we address further in the discussion. Furthermore, provided that only one substitution mechanism is being considered, use of a different calibration would change C_{H_2O} proportionately, and the relationship to a_{H_2O} would not be affected.

The water contents, C_{H_2O}, associated with the [Si], [Mg] and [triv] were fitted by weighted least squares regression with uncertainties in both C_{H_2O} and X_{H_2O} as given in Table 2, to the equation:

$$\ln(C_{H_2O}) = a + b * \ln(X_{H_2O}) \quad (9)$$

where C_{H_2O} is the concentration of water in ppm (μg g^{-1}) for a particular point defect: a and b are constants and X_{H_2O} is the mole fraction of H_2O in the H_2O–NaCl fluids loaded into the capsule of the experiment, and is related to the activity of H_2O by $a_{H_2O} = X_{H_2O}\gamma_{H_2O}$. For the purposes of this immediate discussion, we assume that γ_{H2O}, the activity coefficient, is unity (ideal mixing). This assumption will be revisited below. With this assumption, the constant b is the exponent from Eqs. 5, 6, 7 and 8, and the value derived from the regression provides a means of testing the stoichiometry of the different point defects.

Exponents for [Si], [triv] and [Mg] experiments are 2.5 ± 0.2, 0.6 ± 0.1 and 1.1 ± 0.1, which are close to but consistently higher than the predicted exponents of 2, 0.5 and 1. Such similar values are a strong indication that the substitution stoichiometries given by equilibria 5 to 7 are substantially correct. The data for the [Ti] experiments present the problem that there is substantial overlap of bands associated with [Si] with those that appear in the [Ti] experiments in the wavenumber region 3650–3450 cm^{-1}. This is confirmed by [Mg] experiments, which were performed under identical conditions but without being doped with Ti. Spectra from these forsterite crystals show absorption bands at 3578 cm^{-1} along E||a and 3567 cm^{-1} along E||c, bands which are most prominently observed in experiments conducted at lower silica activity and higher pressure (Lemaire et al. 2004; Mosenfelder et al. 2011). In order to obtain the correct exponent for water associated with Ti, spectra were deconvoluted into 7–8 bands in an effort to isolate the overlapping, defect-specific bands (Fig. 7, Table 4). Following deconvolution, the areas corresponding to both the principal [Ti] bands and subsidiary bands associated with [Si] were calculated (Tables 2 and 3). Regression of these data gives exponents of [Ti] 0.95 ± 0.09, while for [Si], we obtain 2.6 ± 0.4, in good agreement with the value of 2.5 ± 0.2 calculated for olivine from the [Si] experiments. The agreement is evidence that we have successfully deconvoluted the absorbances associated with the [Si] and [Ti] defects from their measured sum.

There is a tendency for the exponents to be somewhat higher than those expected from the stoichiometry of reactions 1 to 4. This is explicable if there is a negative departure from ideal mixing in H_2O–NaCl fluids. The data can be reconciled to the expected values of the exponents if we describe the H_2O–NaCl binary at 1050 °C and 3 GPa by a regular solution model, such that RT ln $\gamma_{H_2O} = W_{H_2O\text{–}NaCl}(1-X_{H_2O})^2$, with an interaction parameter $W_{H_2O\text{–}NaCl}$ of ~−5 kJ/mol. This is not in agreement with the experimental study of Aranovich and Newton (1996), who found that while a_{H_2O} was nearly proportional to X_{H2O} in NaCl–H_2O solutions at 0.2 GPa, with increasing pressure, a_{H_2O} −X_{H_2O} relations tended towards $a_{H_2O} \propto (X_{H_2O})^2$. If this were the relationship for our

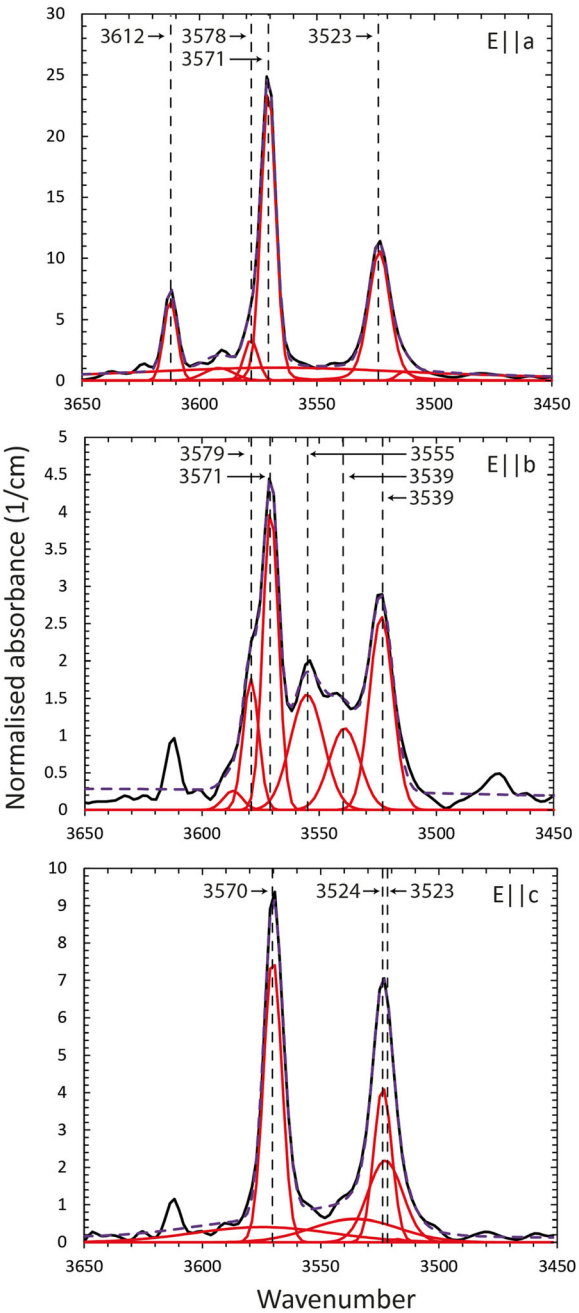

Fig. 7 Examples of deconvoluted spectra along E||a, E||b and E||c for [Ti] experiments. The deconvolution is necessary to isolate the absorbance due to [Ti] from that due to [Si]

Table 4 Calculated water contents associated with each band deconvoluted from the measured spectra of [Ti] experiments. The method used is explained in the text

		E‖a				E‖b						E‖c		
		Wavenumber of band centre (cm^{-1})				Wavenumber of band centre (cm^{-1})						Wavenumber of band centre (cm^{-1})		
		H_2O (ppm)				H_2O (ppm)						H_2O (ppm)		
Experiment	X_{H2O}	3612	3578	3571	3523	3587	3579	3571	3555	3539	3524	3570	3524	3523
62	1	9.7	5.4	35.4	27.0	0.1	3.9	8.9	6.8	4.1	8.1	16.7	9.3	11.7
34	1	10.3	5.6	41.1	26.8	0.6	3.2	7.4	6.1	4.0	7.2	16.2	8.7	9.0
37	1	8.2	4.9	20.6	15.9	0.6	3.4	5.9	6.0	3.5	5.3	12.5	6.9	5.9
79	1	12.3	5.3	14.4	8.5	0.3	3.9	4.6	6.5	3.8	3.6	10.6	4.5	0.0
42	1	6.1	2.7	37.9	28.2	1.3	2.2	8.3	5.6	2.4	7.8	14.1	10.5	6.6
76	0.81	5.0	3.1	33.2	26.6	0.0	2.0	5.8	3.1	1.5	6.9	12.7	10.3	10.5
69	0.7	3.1	2.6	29.6	24.2	0.0	1.2	6.6	2.3	1.0	7.0	10.1	8.2	9.4
70	0.57	1.3	1.1	25.3	16.6	0.2	0.5	5.1	1.1	0.5	4.9	7.9	6.1	5.4
77	0.41	0.6	0.7	17.5	11.6	0.1	0.2	2.9	0.3	0.2	3.0	5.4	4.0	4.1
80	0.22	0.1	0.4	11.4	7.3	0.1	0.1	2.6	0.2	0.0	2.4	3.7	3.1	3.1

experiments, then, although the relative differences between exponent terms for different defects would remain the same, the absolute values would differ, casting doubt on our identifications of their stoichiometries. However, we note that our experiments were conducted at a higher temperature and pressure than the range investigated by Aranovich and Newton (1996), which extends only to 900 °C and 1.5 GPa. It should also be noted that we have not allowed for other components, such as SiO_2, dissolving in H_2O–NaCl fluids, which would lower a_{H_2O} compared to the simple binary.

Composition and water incorporation

The association between olivine composition and water incorporation remains a subject of debate in the literature, particularly the role of certain trace elements, such as Ti and trivalent species such as Fe^{3+}, Al and Cr^{3+}. Experimental studies have shown clear evidence for coupled substitution of hydrogen with these species in simple systems (Berry et al. 2005; Berry et al. 2007a; Faul et al. 2016; Férot and Bolfan-Casanova 2012; Grant et al. 2007a, b; Kovacs et al. 2010), supported by atomistic simulations (Balan et al. 2011; Blanchard et al. 2017; Walker et al. 2007). Furthermore, the FTIR spectra produced by these studies reproduce well the dominant absorbance bands of natural olivine crystals (Berry et al. 2005; Schmädicke et al. 2013; Tollan et al. 2015). However, there are few studies reporting good correlations between trace element composition and water content in natural olivine crystals, leading some to conclude that such incorporation mechanisms are of limited importance (Gaetani et al. 2014; Withers and Hirschmann 2008).

Our study confirms a clear relationship between water content and the presence of Ti and Sc. Of particular significance are the correlations between Ti concentration, water concentration and water activity in [Ti] experiments at both fixed water activity and fixed bulk Ti concentration (Figs. 2 and 8). This indicates that Ti and H are being incorporated together as part of the same point defect, and that the formation of this defect is the dominant method of incorporating both Ti and H in the system studied. Note that Ti concentrations overlap the range found in natural mantle olivines (De Hoog et al. 2010). Extrapolating the trend of H_2O concentration vs. Ti concentration to anhydrous conditions gives a Ti

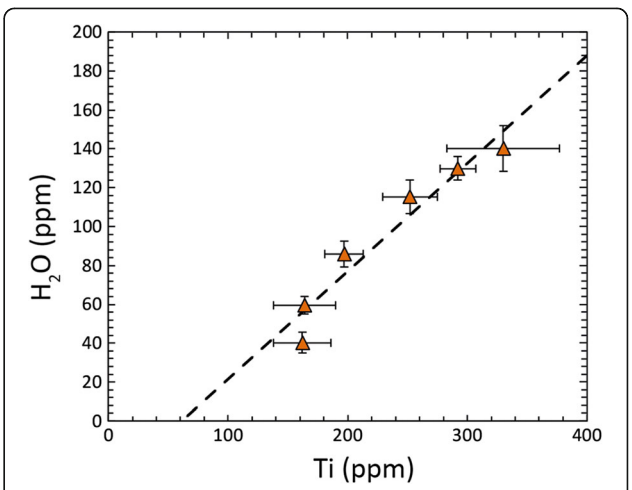

Fig. 8 Variation of H_2O concentration (C_{H_2O}) with Ti concentration for [Ti] experiments conducted at variable a_{H_2O}. The *dashed line* is a best fit through the deconvoluted data

concentration of ~60 ppm (Fig. 8), which is close to the maximum solubility of Ti in olivine under anhydrous conditions at the same temperature and pressure, as estimated from the experimental study of Hermann et al. (2005). This illustrates how Ti solubility in olivine is dramatically increased at high water activities. Converting H_2O and Ti to molar concentrations allows a further opportunity to assess the relationship between these two species (Fig. 9). The stoichiometry of Ti-clinohumite, $MgTi(OH)_2O_2$, requires two moles of OH (or one mole of H_2O) for every mole of Ti. Taking [Ti] experiments with a constant water activity of 1 but variable Ti concentration in olivine, we find that the trend of the data is very close to the 1:1 line (moles of Ti to moles of H_2O), consistent with this stoichiometry. Furthermore, this indicates that at water, saturated conditions ($a_{H_2O} = 1$) at 3 GPa and 1050 °C, essentially all Ti substitutes by the Ti-clinohumite point-defect mechanism, as opposed to tetrahedral Ti as in the Mg_2TiO_4 substitution (Berry et al. 2007b). The latter substitution becomes more important at higher temperatures and lower pressures (Hermann et al. 2005) and with increasing Fe content (O'Neill 1998). Finally, the good agreement between molar concentrations of Ti and H_2O is a strong indication that the absorption coefficient of Bell et al. (2003) is reliable for this particular defect. The Bell value was determined using olivines with identical spectra to our [Ti] experiments. Likewise, the identical value obtained from [Ti] experiments by Kovacs et al. (2010) is also validated.

Similar trends can also be observed for the [triv] experiments, where water activity was held constant and bulk Sc concentration varied. In this case, there is a good positive correlation between Sc concentration and H_2O concentration; however, when converted to molar concentrations, there is a deviation of approximately one third away from the expected Sc:H_2O molar ratio, such that there is more water than expected, given the Sc concentration. This deviation is consistent with the results of the study by Berry et al. (2007a), implying that this is not isolated just to Sc but to all R^{3+} cations (Fig. 10). We suggest that the simplest explanation for this is that the absorption coefficient used is not appropriate for this particular defect and should be increased by one third from the values reported by Bell et al. (2003) and Kovacs et al. (2010) and close to the value reported by Withers et al. (2012), in order to compensate for the excess water calculated here and by Berry et al. (2007a). This is also consistent with predictions from theoretical calculations for this type of defect (Blanchard et al. 2017), although the absolute value obtained in that study is somewhat unlikely. Since this defect is relatively common in natural olivines and thus a major contributor to mantle water storage (Tollan et al. 2015), an experimental study specifically designed to determine the absorption coefficient for this defect is required.

A further result that contrasts with the [Ti] experiments is that there is no correlation between the very

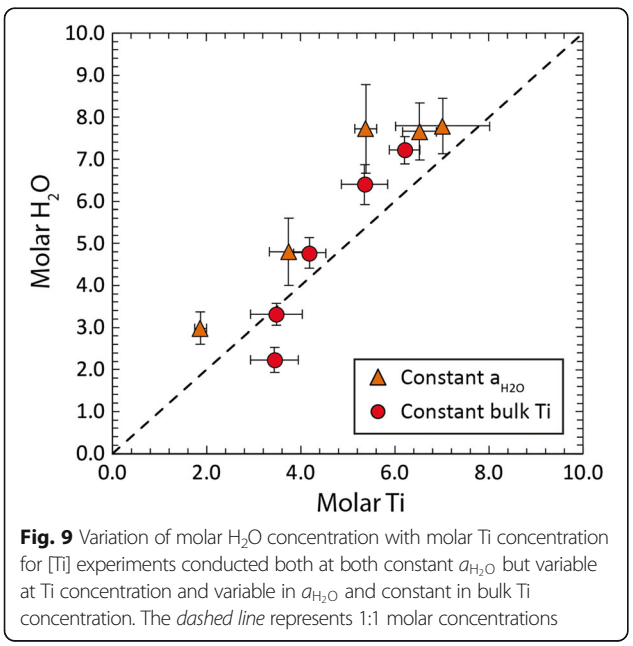

Fig. 9 Variation of molar H_2O concentration with molar Ti concentration for [Ti] experiments conducted both at both constant a_{H_2O} but variable at Ti concentration and variable in a_{H_2O} and constant in bulk Ti concentration. The *dashed line* represents 1:1 molar concentrations

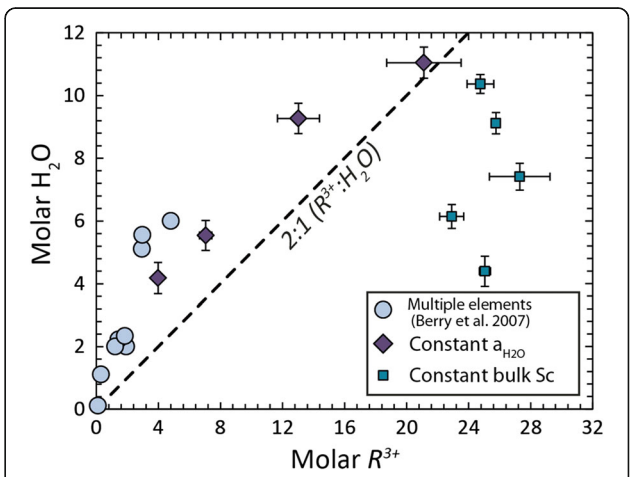

Fig. 10 Variation of molar H_2O concentration with molar Sc concentration for [triv] experiments conducted at constant water activity but variable in Sc concentration and at fixed bulk Sc concentration. Note that the latter experiments show no correlation between forsterite water concentration and Sc concentration, for reasons discussed in the text. For comparison, we have also plotted data from Berry et al. (2007a), which were similar experiments but at 1400 °C and 1.5 GPa and performed with a variety of trivalent cations in addition to Sc (Al, V, Ga, Y, In, Gd, Dy, Tm and Lu). Both sets of data confirm a consistent increase of C_{H_2O} with the availability of an R^{3+} cation at fixed water activity, but the deviation from the expected stoichiometry for the substitution may indicate that the absorption coefficient used in this study to calculate C_{H_2O} is in error; the value obtained by Withers et al. (2012) may be more appropriate (see text for further discussion)

high concentrations of Sc and H_2O concentration in the series at variable water activity, suggesting that another charge-balancing mechanism for Sc is operating in addition to the hydrous defect proposed here. Under anhydrous conditions, considerable Sc in olivine can be charge-balanced by an octahedral site vacancy (Spandler and O'Neill 2010) or, alternatively, Na^+ could be incorporated from the salt-water solution and charge-balance Sc instead of H^+. The latter would be increasingly important at lower water activities, where the $NaCl/H_2O$ ratio of the fluid increases substantially. But Grant and Wood (2010) found little evidence for coupled substitution of Na and Sc, so this reaction seems unlikely. It is possible that other charge-balancing species (such as Li) were present as contaminants in the salt; this would require further work to demonstrate.

Comparisons with other studies

Matveev et al. (2001) conducted experiments on natural olivines from Mount Porndon (initially $Fo_{90–91}$) at a range of water activities, controlled by diluting H_2O with CO_2 at 1300 °C and 2 GPa. Although their experiments were designed to be M-type, the olivine partially recrystallised to some extent in all runs, and FTIR spectra were reported only for the recrystallised material, using the marked change in Fo content (to ~$Fo_{96–97}$) as a discriminant. Their results are therefore for G-type experiments, which explain why they were able to obtain completely different FTIR spectra in orthopyroxene-buffered experiments from magnesiowüstite-buffered experiments, as in this study. They found a factor of 1.3 decrease in water concentration in olivine over the range in X_{H_2O} from 1.0 to 0.3, in four orthopyroxene-buffered experiments. Inspection of their spectra shows that the [triv] defect dominates the total absorbance, and we can therefore directly compare their results to ours for this defect, but with the caveat that the trivalent cations associated with the [triv] substitution in the natural olivines are likely Fe^{3+} or/and Cr^{3+} (cf. Tollan et al. 2015) rather than Sc. Considerable Fe^{3+} in their olivines is expected given the relatively high oxygen fugacities of their experiments, achieved using the Re–ReO_2 buffer. The exponent for this defect derived from their data (following the same data-fitting procedure as for this study) is 0.58 ± 0.21, which is identical within uncertainty to the exponent calculated for the [triv] substitution in this study, supporting our hypothesis that the configurational entropy of the [triv] substitution is independent of the identity of the trivalent cation. The [triv] substitution was absent in the spectra from their magnesiowüstite-buffered experiments, although these were conducted at the same oxygen fugacity (Re–ReO_2); this observation confirms the role of high a_{SiO_2} in promoting this substitution, according to reaction (3). Their attribution of the [Si] substitution mechanism to the FTIR spectra of natural olivines published by Miller et al. (1987) was a mistake due to confusing the [Si] substitution in their experiments with the [Ti] substitution in the natural crystals. In the experiments, the Ti in the starting crystals of Mount Porndon olivine, which is low anyway (~20 ppm in an example analysed by Eggins et al. 1998), would have been lost during recrystallisation, while the infrared fingerprint of the [Ti] substitution was only recognised later (Berry et al. 2005).

Gaetani et al. (2014) performed what they assumed were M-type experiments on San Carlos olivine, but with re-equilibration of fO_2-sensitive defects. Only the orthopyroxene-buffered condition was investigated. They used mixtures of H_2O and CO_2 to vary a_{H_2O} but explored only three conditions $(X_{H_2O} = 1, 0.855, 0.185)$. There is a factor of ~2.5 difference between the lowest and highest water concentrations. Given that their published FTIR spectra show the [Ti], [triv] and [Mg] substitutions, this is in good agreement with our results. Gaetani et al. (2014) also demonstrate a decrease in intensity of the [triv] peaks between experiments at high and low fO_2, which suggests that the [triv] substitution was mainly associated with Fe^{3+}, which re-equilibrated during the hydroxylation. Interestingly, in M-type experiments, such reduction may be mediated by the fugacity of H_2 if the reaction occurs without diffusion of other elements:

$$Fe^{3+}HSiO_4 + 0.5\ H_2 = Fe^{2+}H_2SiO_4 \quad (10)$$

Here, the component $Fe^{2+}H_2SiO_4$ represents essentially the same substitution mechanism in ferromagnesian olivines that we refer to as [Mg] in forsterite (Eq. 2). This reaction suggests that reduction of the Fe^{3+} [triv] substitution would increase the [Mg] substitution in M-type experiments, but as the olivines used by Gaetani et al. (2014) differed in composition, and the partitioning of $C_{H_2O}^{Total}$ amongst the three different substitution mechanisms was not reported, this hypothesis cannot yet be tested.

Yang et al. (2014) also used different ratios of H_2O and CO_2, finding a difference of a factor of 2 between values of C_{H_2O} in olivines from experiments with pure H_2O and those with $H_2O–CO_2$, but changing X_{CO2} from 0.22–0.50 apparently had no effect on the water solubility. This observation disagrees with those of Matveev et al. (2001) and Gaetani et al. (2014). Otsuka and Karato (2011) studied the effect of variable a_{H_2O} on water in San Carlos olivine in M-type experiments at 1000 °C and 5 GPa by using two three-phase assemblages involving a hydrous phase in the system MgO–SiO_2–H_2O, which produces known a_{H_2O} in the absence of a fluid phase, plus one experiment with H_2O fluid $(a_{H_2O} \sim 1)$. Thus, three values of a_{H_2O} were investigated. They observed that $C_{H_2O}^{Total} \propto a_{H_2O}$ (i.e. the exponent was 1), but their

published polarised infrared spectra show that the hydroxyl in their run products is held by a combination of both the [Si] and the [triv] mechanisms. Deconvolution of the spectra would be needed to see if $C_{H_2O}^{[Si]} \propto a_{H_2O}{}^2$ and $C_{H_2O}^{[triv]} \propto a_{H_2O}{}^{0.5}$. The proportion of the [Si] substitution did increase with a_{H_2O}, in agreement at least qualitatively with the results of this study. This interpretation is also supported by the reported changes in the anisotropy of the absorption with a_{H_2O}.

Assignment of infrared absorption bands to substitution mechanisms

Our data also provides new evidence on the interpretation of infrared bands at wavenumbers greater than 3450 cm^{-1}, which typically dominate the spectra of natural olivines. There has been debate in the literature concerning whether silicon vacancies or magnesium vacancies are the main host of water in olivine. Zhao et al. (2004), Mosenfelder et al. (2006), Kohlstedt (2006), Bali et al. (2008) and Otsuka and Karato (2011) suggest that water associated with Mg vacancies is the most important incorporation mechanism and is responsible for the generation of high wavenumber bands, based on relationships between water solubility and fH_2O in experimental studies conducted over a broad range of conditions. A similar assignment has also been made by Smyth et al. (2006) through X-ray site occupancy refinement measurements on very water-rich samples equilibrated at high pressure and high a_{H_2O}.

On the other hand, Matveev et al. (2001), Lemaire et al. (2004), Berry et al. (2005, 2007a), Walker et al. (2007), Kovacs et al. (2010), Balan et al. (2011), Umemoto et al. (2011) and Ingrin et al. (2013) concluded that high wavenumber bands are instead due to hydrated Si vacancies, based on experimental studies at a range of silica activities, atomistic simulations of different hydroxyl configurations and the response of absorption bands to heating from liquid nitrogen temperatures. Furthermore, Blanchard et al. (2009), Umemoto et al. (2011) and Ingrin et al. (2013) pointed out that the use of the empirical relationship between OH frequencies and O–O bond distances by Smyth et al. (2006) is not valid for predicting site occupancy of hydroxyl groups in nominally anhydrous phases, since such a correlation was established for hydrous phases. Most recently, Xue et al. (2017) used ^1H NMR to determine the H positions in forsterite with 0.5 wt% H_2O, synthesised at 1200 °C and 12 GPa. They concluded that "this study has provided unambiguous evidence supporting that hydrogen is incorporated in forsterite at relatively high pressure dominantly as (4H)Si defects, with (2H)M1 defects playing only a very minor role".

By showing again that the appropriate compositional variations yield forsterite (or olivine) with different O–H infrared spectra, the results presented here confirm these latter interpretations of the identities of the substitution mechanisms of H_2O in olivine. The fact that the concentrations of hydroxyl, C_{H_2O}, in these different substitutions depend on a_{H_2O} in different ways that accord with the expected stoichiometry of the mechanisms (Eqs. 5, 6, 7 and 8) introduces a new line of supporting evidence for the identification of the substitution mechanisms, as does the variation of $C_{H_2O}^{[Ti]}$ with the concentration of Ti, and $C_{H_2O}^{[triv]}$ with the concentration of Sc (Fig. 10). The substitution mechanism associated with Mg site vacancies, [Mg], is quantitatively minor even at high a_{SiO_2} (buffered by enstatite) and unobservable at low a_{SiO_2} (buffered by magnesiowüstite), thereby refuting assertions that this mechanism is the main one by which H_2O substitutes into olivine. Nevertheless, the results on the [Mg] substitution are of considerable theoretical interest, because they show that the concentration of H_2O associated with this mechanism is the same at a given a_{H_2O} in the Sc- and Ti-doped forsterites as in the undoped forsterite, despite the fact that the total concentrations of H_2O $\left(C_{H_2O}^{Total}\right)$ in the latter experiments are much higher (Fig. 2d). This confirms that the concentrations of H_2O by the different mechanisms are additive, although from thermodynamic principals it is hard to conceive how this could be otherwise. Therefore, the total concentration of water in forsterite or olivine must be described by an equation of the type:

$$C_{H_2O}^{Total} = C_{H_2O}^{[Si]} + C_{H_2O}^{[Mg]} + C_{H_2O}^{[Ti]} + \sum_{R^{3+}} C_{H_2O}^{[triv]} \qquad (11)$$

where the R^{3+} cations of importance in natural olivines are likely Fe^{3+} and Cr^{3+} (Tollan et al. 2015) and perhaps Al (Grant et al. 2007a).

For each substitution mechanism X, there is a separate equilibrium constant $K^{[X]}$ that relates $C_{H_2O}^{[X]}$ to $f(H_2O)$ and a_{SiO_2} in different ways (Eqs. 5, 6, 7 and 8), and each $K^{[X]}$ is a function of temperature and pressure. In addition, the [Ti] and [triv] substitutions depend on the concentrations of Ti and relevant R^{3+} cations, hence the activities of TiO_2 and the $R^{3+}O_{1.5}$ components in a system at global equilibrium. The $R^{3+}O_{1.5}$ components important in natural olivines are likely mainly $Fe^{3+}O_{1.5}$ and $Cr^{3+}O_{1.5}$ (Tollan et al. 2015; Blanchard et al. 2017), which are both redox-sensitive and depend on fO_2. It might be tempting to develop a single constitutive equation for the solubility of water in olivine as a function of these variables, but the convenience of this should be balanced against the guarantee that it would produce the wrong answers (Ingrin et al. 2013). A sufficient equation necessitates the parameterisation of each term on the right-hand side of Eq. 11 separately as a function of their relevant variables.

Implications for the assessment of water incorporation in mantle olivine

Not addressed in this study are the effects of temperature and pressure on the individual substitution mechanisms, but it would be extraordinary if the solubility of water in the four different mechanisms did not respond very differently to these variables. From the thermodynamic perspective, the effect of pressure acts in three ways at a given a_{H_2O} and a_{SiO_2}: (1) the increase of $f(H_2O)^\circ$ with pressure; (2) the effect that $f(H_2O)^\circ$ has through the stoichiometries of the reactions (reactions 1 to 4 and Eqs. 5, 6, 7 and 8); and (3) the effect on the equilibrium constants (Eqs. 5, 6, 7 and 8). As regards this third factor, the effect of pressure at constant $f(H_2O)$ (NB not constant $f(H_2O)^\circ$) is:

$$\Delta \ln K = \int_{P1}^{P_2} \Delta \overline{V}_{solids}(P,T)dP \quad (12)$$

where $\Delta\overline{V}_{solids}$ is the change in partial molar volume of the solid components. For the example of the [Si] mechanism (reaction 1), $\Delta\overline{V}_{solids}$ is given by:

$$\Delta \overline{V}^{[Si]}_{solids} = \overline{V}^{olivine}_{Mg_2H_4O_4} - V^{olivine}_{Mg_2SiO_4} - V_{SiO_2} \quad (13)$$

Here, $\overline{V}^{olivine}_{Mg_2H_4O_4}$ is the partial molar volume of the $Mg_2H_4O_4$ component in the olivine, and V_{SiO_2} is the effective molar volume of the system, as determined by the coexisting phases. The standard states are the conventional ones of the pure components at the P, T of interest for the solid phases, and pure H_2O as an ideal gas at T and 1 bar. The value of $\overline{V}^{olivine}_{Mg_2H_4O_4}$ (298,1) may be calculated from the data in Smyth et al. (2006) as 45.2 cm^3/mol, by recalculating the H_2O contents of hydrous forsterites given in Table 2 to mole fractions of the $Mg_2H_4O_4$ component, and extrapolating linearly to this end-member. Hence, with V_{SiO_2} (298,1) = 19.0 cm^3/mol (from Mg_2SiO_4 + $Mg_2Si_2O_6$) and $V^{olivine}_{Mg_2SiO_4}$ (298,1) = 43.7 cm^3/mol, all from Holland and Powell (2011), we calculate $\Delta\overline{V}_{solids^{[Si]}}(298,1) = 20.5\ cm^3/mol$. However, what is really needed is to compare the response of the [Si] substitution to pressure with those of [Mg], [Ti] and [triv], which requires the partial molar volumes of the components MgH_2SiO_4 and $MgTiH_2O_4$, and the relevant $R^{3+}HSiO_4$ components, which are at present unknown.

In contrast, the differential effect of the change in $f(H_2O)^\circ$ with pressure comes simply from the stoichiometry of the reaction: increasing pressure will favour the [Si] substitution, because $C_{H_2O} \propto f(H_2O)^2$. That the [Si] mechanism is indeed the dominant mechanism in experiments with a_{H_2O} ~1 at P >> 3 GPa, even at high a_{SiO_2} (buffered by orthopyroxene) is evident from several experimental studies (Kohlstedt et al. 1996; Mosenfelder et al. 2006; Withers and Hirschmann 2008). However, decreasing a_{H_2O} at any pressure and temperature will decrease the proportion of [Si] relative to [Mg], [Ti] and especially [triv]. Higher temperatures should favour the mechanisms with higher configurational entropy, if differences in vibrational entropies are of subsidiary importance (Walker et al. 2007). With this assumption, the relative amounts of water associated with the different defects should increase with increasing temperature in the reverse order from the effect of pressure at a_{H_2O} ~1: [triv] > [Mg] ~ [Ti] > [Si] (Eqs. 1, 2, 3 and 4), other variables remaining constant.

We reiterate the point made by Ingrin et al. (2013), who emphasised that water incorporation into olivine cannot be described by a single solubility law. The existence of the four main solubility mechanisms with their different controlling stoichiometries mandates that the relationship between C_{H_2O} and the intensive thermodynamic variables of temperature, pressure, fH_2O and compositional variables requires four separate terms, one for each mechanism. Quantifying water substitution in olivine must also allow for the availability of Ti and the trivalent cations, particularly Fe^{3+}, whose concentration is sensitive to fO_2. Varying a_{SiO_2} also affects substitution mechanisms in different ways. Obviously, increasing a_{SiO_2} increases Mg vacancies but decreases Si vacancies and vice versa, but increasing a_{SiO_2} should also promote the [triv] substitution but decrease [Ti] (Eqs. 3 and 4). The values of a_{SiO_2} as buffered at low or high values by magnesiowüstite or pyroxene, respectively, also both change with P and T. The effect of the major element compositional variable Mg/Fe^{2+} on each mechanism also requires systematic study.

The fact that there are three ways by which increasing pressure at constant given a_{H_2O} and relative a_{SiO_2} changes $C^{[X]}_{H_2O}$ for each of the four substitution mechanisms means that it is difficult to deduce the nature of the substitution mechanism from the change of $C^{[X]}_{H_2O}$ with pressure; it would be even more difficult to deduce how water dissolves in olivine with the change of $C^{Total}_{H_2O}$ with pressure.

Interactions between the four defect mechanisms should also be taken into account in the interpretation of the water contents of natural olivines and their FTIR spectra. The speciation of water in olivine observed in simple-system experiments may not be preserved in natural olivines because of rearrangements on cooling and/or decompression. Where this occurs without mass transfer of components into or out of the olivine by diffusion, such rearrangements may be rapid. To give one example, it is possible that water may transfer from the [triv] mechanism to the [Ti] mechanism according to the reaction:

$$4/3R^{3+}HSiO_4 + 2/3\ Mg_2TiO_4 = {R^{3+}}_{4/3}SiO_4 + 2/3\ MgTiH_2O_4 + 1/3\ Mg_2SiO_4 \quad (14)$$

where all components are in olivine. The $R^{3+}_{4/3}SiO_4$ component is the anhydrous substitution of R^{3+} into olivine, charge-balanced by octahedral site vacancies (Evans et al. 2008), while the Mg_2TiO_4 component is the anhydrous substitution of Ti for Si in olivine studied by Hermann et al. (2005). Therefore, the observation that [Ti] is the dominant mechanism for water incorporation in olivine from San Carlos xenoliths (Berry et al. 2005) may reflect internal re-equilibration during cooling to some extent as yet unknown. Loss of water from olivine, which has often been inferred from both phenocryst olivines in magmas during eruption, or from olivines in xenoliths during their exhumation (e.g. Tollan et al. 2015 and references therein), may also affect speciation. Water loss changes a_{SiO_2} (inter alia), hence the point-defect structure of the olivine, in different ways according to the different substitution mechanisms (Eqs. 1, 2, 3 and 4). The effects of this are further complicated by the different rates of diffusion of H associated with the different substitution mechanisms (Padrón-Navarta et al. 2014).

Conclusions

This study presents the results of G-type experiments at one condition of temperature and pressure, namely 1050 °C and 3 GPa, which confirm the identities of the four main substitution mechanisms by which water is likely to be incorporated into mainstream mantle olivines. The results demonstrate the role that a_{H_2O} plays in determining which mechanisms are significant at the experimental condition, but from the stoichiometries of the substitution mechanisms, the same principle should apply at other pressures and temperatures. Evaluating water solubilities is not straightforward because it depends on the mechanisms by which water is incorporated (the type of hydrous defect), which in turn is dictated by other factors, most notably composition and silica activity. The consequence of this is that under otherwise identical conditions, higher water activities will favour hydrated silicon vacancies ([Si]) over other defects. Conversely, at low water activities, the ratio of hydrated silicon vacancies to other hydrous defects will be much lower. This has profound impacts for our understanding of water storage in the mantle and interpretation of measurements of natural olivine from different mantle domains. For example, the absence of the infrared absorption bands associated with the [Si] mechanism does not necessarily indicate high silica activity but could be due to low water activities, as expected in most mantle environments (Bali et al. 2008; Lamb and Popp 2009). This is highlighted by our observation that the [Si] substitution features prominently in enstatite-buffered experiments at high pressures and high a_{H2O}, even dominating total absorbance (Smyth et al. 2006). In order to understand the role of water in the mantle, careful consideration needs to be given to several factors that have hitherto been underappreciated, including the limitations on a_{H_2O} and the role of minor components, especially Ti and the more abundant R^{3+} cations, Fe^{3+} and Cr^{3+}.

Acknowledgements

We thank Dean Scott and Dave Clark for their tireless efforts maintaining the running of the experimental laboratories, Jung Park for his assistance with the LA-ICP-MS measurements and both Mike Jollands and Alberto Padrón-Navarta for their assistance with the FTIR and many valuable and fruitful discussions. We thank the two anonymous reviewers and Shun-ichiro Karato for his review and editorial handling.

Funding

We gratefully acknowledge the Australian Research Council (ARC) support through DP110103134 to JH and HON, and FL130100066 to HON, which partly supported PT during the final stages of this project. RS acknowledges an Australian Postgraduate Award.

Authors' contributions

The project was conceived by HON and JH, with the experiments and analyses conducted by RS. PT processed and modelled the data. PT and HON fit the data to the thermodynamic model. PT and HON wrote the manuscript with help from JH. All authors read and approved the final manuscript.

Competing interests

The authors declare that they have no competing interests.

Publisher's Note

Author details

[1]Research School of Earth Sciences, The Australian National University, Building 142, Mills Road, Canberra, ACT 2601, Australia. [2]Institute of Geological Sciences, Universität Bern, Bern 3012, Switzerland.

Received: 26 December 2016 Accepted: 23 April 2017
Published online: 09 May 2017

References

Aranovich LY, Newton RC (1996) H_2O activity in concentrated NaCl solutions at high pressures and temperatures measured by the brucite-pericalse equilibrium. Contrib Mineral Petrol 125:200–212

Aubaud C et al (2007) Intercalibration of FTIR and SIMS for hydrogen measurements in glasses and nominally anhydrous minerals. Am Mineral 92(5–6):811–828

Bai Q, Kohlstedt DL (1993) Effects of chemical environment on the solubility and incorporation mechanism for hydrogen in olivine. Phys Chem Miner 19:460–471

Balan E, Ingrin J, Delattre S, Kovács I, Blanchard M (2011) Theoretical infrared spectrum of OH-defects in forsterite. Eur J Mineral 23(3):285–292

Bali E, Bolfan-Casanova N, Koga KT (2008) Pressure and temperature dependence of H solubility in forsterite: an implication to water activity in the Earth interior. Earth Planet Sci Lett 268(3–4):354–363

Bell DR, Rossman GR, Maldener J, Endisch D, Rauch F (2003) Hydroxide in olivine: a quantitative determination of the absolute amount and calibration of the IR spectrum. J Geophys Res 108

Berry AJ, Hermann J, O'Neill HSC, Foran GJ (2005) Fingerprinting the water site in mantle olivine. Geology 33(11):869

Berry AJ, O'Neill HSC, Hermann J, Scott DR (2007a) The infrared signature of water associated with trivalent cations in olivine. Earth Planet Sci Lett 261(1–2):134–142
Berry AJ, Walker AM, Hermann J, O'Neill HSC, Foran GJ, Gale JD (2007b) Titanium substitution mechanisms in forsterite. Chem Geol 242(1–2):176–186
Blanchard M, Balan E, Wright K (2009) Incorporation of water in iron-free ringwoodite: a first-principles study. Am Mineral 94(1):83–89
Blanchard M, Ingrin J, Balan E, Kovács I, Withers AC (2017) Effect of iron and trivalent cations on OH defects in olivine. Am Mineral 102(2):302–311
De Hoog JCM, Gall L, Cornell DH (2010) Trace-element geochemistry of mantle olivine and application to mantle petrogenesis and geothermobarometry. Chem Geol 270(1–4):196–215
Demouchy S, Mackwell S (2006) Mechanisms of hydrogen incorporation and diffusion in iron-bearing olivine. Phys Chem Miner 33:347–355
Demouchy S, Mackwell SJ, Kohlstedt DL (2007) Influence of hydrogen on Fe–Mg interdiffusion in (Mg, Fe)O and implications for Earth's lower mantle. Contrib Mineral Petrol 154(3):279–289
Denis CMM, Demouchy S, Shaw CSJ (2013) Evidence of dehydration in peridotites from Eifel Volcanic Field and estimates of the rate of magma ascent. J Volcanol Geotherm Res 258:85–99
Eggins SM, Rudnick RL, McDonough WF (1998) The composition of peridotites and their minerals: a laser-ablation ICP-MS study. Earth Planet Sci Lett 154:53–71
Evans TM, O'Neill HSC, Tuff J (2008) The influence of melt composition on the partitioning of REEs, Y, Sc, Zr and Al between forsterite and melt in the system CMAS. Geochim Cosmochim Acta 72:5708–5721
Faul UH, Cline CJ, David EC, Berry AJ, Jackson I (2016) Titanium-hydroxyl defect-controlled rheology of the Earth's upper mantle. Earth Planet Sci Lett 452: 227–237
Férot A, Bolfan-Casanova N (2012) Water storage capacity in olivine and pyroxene to 14 GPa: implications for the water content of the Earth's upper mantle and nature of seismic discontinuities. Earth Planet Sci Lett 349–350:218–230
Gaetani GA et al (2014) Hydration of mantle olivine under variable water and oxygen fugacity conditions. Contrib Mineral Petrol 167(2):965
Grant KJ, Wood BJ (2010) Experimental study of the incorporation of Li, Sc, Al and other trace elements into olivine. Geochim Cosmochim Acta 74(8):2412–2428
Grant KJ, Kohn SC, Brooker RA (2007a) The partitioning of water between olivine, orthopyroxene and melt synthesised in the system albite-forsterite-H_20. Earth and Planet Sci 260: 227–241.
Grant KJ, Brooker RA, Kohn SC, Wood BJ (2007b) The effect of oxygen fugacity on hydroxyl concentrations and speciation in olivine: implications for water solubility in the upper mantle. Earth Planet Sci Lett 261(1–2):217–229
Green DH, Hibberson WO, Kovacs I, Rosenthal A (2010) Water and its influence on the lithosphere-asthenosphere boundary. Nature 467(7314):448–451
Hermann J, O'Neill HSC, Berry AJ (2005) Titanium solubility in olivine in the system TiO_2-MgO-SiO_2: no evidence for an ultra-deep origin of Ti-bearing olivine. Contrib Mineral Petrol 148:746–760
Holland TJB, Powell R (2011) An improved and extended internally consistent thermodynamic dataset for phases of petrological interest, involving a new equation of state for solids. J Metamorph Geol 29:333–383
Ingrin J et al (2013) Low-temperature evolution of OH bands in synthetic forsterite, implication for the nature of H defects at high pressure. Phys Chem Miner 40(6):499–510
Ingrin J, Kovács I, Deloule E, Balan E, Blanchard M, Kohn SC, Hermann J (2014) Identification of hydrogen defects linked to boron substitution in synthetic forsterite and natural olivine. Am Mineral 99:2138–2141
Jollands MC, Padrón-Navarta JA, Hermann J, O'Neill HSC (2016) Hydrogen diffusion in Ti-doped forsterite and the preservation of metastable point defects. Am Mineral 101(7–8):1571–1583
Karato S-I, Wang D (2013) Electrical conductivity of minerals and rocks. In: Karato S-I (ed) Physics and Chemistry of the Deep Earth. Wiley-Blackwell, New York, pp 145–182
Karato S-I, Paterson MS, FitzGerald JD (1986) Rheology of synthetic olivine aggregates: Influence of grain size and water. J Geophys Res 91(B8):8151
Kohlstedt DL (2006) The role of water in high-temperature rock deformation. Rev Mineral Geochem 62:377–396
Kohlstedt DL, Keppler H, Rubie DC (1996) Solubility of water in the α, β and γ phases of (Mg, Fe)2SiO_4. Contrib Mineral Petrol 123:345–357
Kovacs I et al (2008) Quantitative absorbance spectroscopy with unpolarized light: Part II. Experimental evaluation and development of a protocol for quantitative analysis of mineral IR spectra. Am Mineral 93(5–6):765–778
Kovacs I, O'Neill HSC, Hermann J, Hauri EH (2010) Site-specific infrared O-H absorption coefficients for water substitution into olivine. Am Mineral 95(2–3):292–299
Lamb WM, Popp RK (2009) Amphibole equilibria in mantle rocks: determining values of mantle aH_2O and implications for mantle H_2O contents. Am Mineral 94(1):41–52
Lemaire C, Kohn SC, Brooker RA (2004) The effect of silica activity on the incorporation mechanisms of water in synthetic forsterite: a polarised infrared spectroscopic study. Contrib Mineral Petrol 147(1):48–57
Mackwell SJ, Kohlstedt DL (1990) Diffusion of hydrogen in olivine: implications for water in the mantle. J Geophys Res 95:5079–5088
Mallmann G, O'Neill HSC (2009) The crystal/melt partitioning of V during mantle melting as a function of oxygen fugacity compared with some other elements (Al, P, Ca, Sc, Ti, Cr, Fe, Ga, Y, Zr and Nb). J Petrol 50(9):1765–1794
Matveev S, O'Neill HSC, Ballhaus C, Taylor WR, Green DH (2001) Effect of silica activity on OH^- IR spectra of olivine: implications for low-$aSiO_2$ mantle metasomatism. J Petrol 42(4):721–729
Mei S, Kohlstedt DL (2000) Influence of water on plastic deformation of olivine aggregates: 1. Diffusion creep regime. J Geophys Res Solid Earth 105(B9): 21457–21469
Miller GH, Rossman GR, Harlow GE (1987) The natural occurrence of hydroxide in olivine. Phys Chem Miner 14:461–472
Mosenfelder JL, Deligne NI, Asmiow PD, Rossman GR (2006) Hydrogen incorporation in olivine from 2-12 GPa. Am Mineral 91:285–294
Mosenfelder JL et al (2011) Analysis of hydrogen in olivine by SIMS: evaluation of standards and protocol. Am Mineral 96(11–12):1725–1741
O'Neill HSC (1998) Partitioning of Fe and Mn between ilmenite and olivine at 1100 °C: constraints on the thermodynamic mixing properties of (Fe, Mn)TiO_3 ilmenite solid solutions. Contrib Mineral Petrol 133:284–296
Otsuka K, Karato S-I (2011) Control of the water fugacity at high pressures and temperatures: applications to the incorporation mechanisms of water in olivine. Phys Earth Planet Inter 189(1–2):27–33
Padrón-Navarta JA, Hermann J, O'Neill HSC (2014) Site-specific hydrogen diffusion rates in forsterite. Earth Planet Sci Lett 392:100–112
Pownceby MI, O'Neill HSC (2000) Thermodynamic data from redox reactions at high temperatures. VI. Thermodynamic properties of CoO–MnO solid solutions from emf measurements. Contrib Mineral Petrol 140(1):28–39
Sambridge M, Gerald JF, Kovacs I, O'Neill HSC, Hermann J (2008) Quantitative absorbance spectroscopy with unpolarized light: Part I. Physical and mathematical development. Am Mineral 93(5–6):751–764
Schmädicke E, Gose J, Witt-Eickschen G, Bratz H (2013) Olivine from spinel peridotite xenoliths: hydroxyl incorporation and mineral composition. Am Mineral 98(10):1870–1880
Shen T, Hermann J, Zhang L, Padrón-Navarta JA, Chen J (2014) FTIR spectroscopy of Ti-chondrodite, Ti-clinohumite, and olivine in deeply subducted serpentinites and implications for the deep water cycle. Contrib Mineral Petrol 167:992–1009
Smyth JR, Frost DJ, Nestola F, Holl CM, Bromiley G (2006) Olivine hydration in the deep upper mantle: effects of temperature and silica activity. Geophys Res Lett 33(15)
Soustelle V, Tommasi A, Demouchy S, Ionov DA (2010) Deformation and fluid-rock interaction in the supra-subduction mantle: microstructures and water contents in peridotite xenoliths from the Avacha Volcano, Kamchatka. J Petrol 51(1–2):363–394
Soustelle V, Tommasi A, Demouchy S, Franz L (2013) Melt-rock interactions, deformation, hydration and seismic properties in the sub-arc lithospheric mantle inferred from xenoliths from seamounts near Lihir, Papua New Guinea. Tectonophysics 608:330–345
Spandler C, O'Neill HSC (2010) Diffusion and partition coefficients of minor and trace elements in San Carlos olivine at 1,300 °C with some geochemical implications. Contrib Mineral Petrol 159(6):791–818
Tollan PME, O'Neill HSC, Hermann J, Benedictus A, Arculus RJ (2015) Frozen melt–rock reaction in a peridotite xenolith from sub-arc mantle recorded by diffusion of trace elements and water in olivine. Earth Planet Sci Lett 422:169–181
Umemoto K, Wentzcovitch RM, Hirschmann MM, Kohlstedt DL, Withers AC (2011) A first-principles investigation of hydrous defects and IR frequencies in forsterite: The case for Si vacancies. Am Mineral 96(10):1475–1479
Walker AM, Hermann J, Berry AJ, O'Neill HSC (2007) Three water sites in upper mantle olivine and the role of titanium in the water weakening mechanism. J Geophys Res 112(B5)
Withers AC, Hirschmann MM (2008) Influence of temperature, composition, silica activity and oxygen fugacity on the H_2O storage capacity of olivine at 8 GPa. Contrib Mineral Petrol 156(5):595–605

Withers AC, Bureau H, Raepsaet C, Hirschmann MM (2012) Calibration of infrared spectroscopy by elastic recoil detection analysis of H in synthetic olivine. Chem Geol 334:92–98

Xue X, Kanzaki M, Turner D, Loroch D (2017) Hydrogen incorporation mechanisms in forsterite: New insights from ^{1}H and ^{29}Si NMR spectroscopy and first-principles calculation. Am Mineral 102:519–536

Yang X, Liu D, Xia Q (2014) CO_2-induced small water solubility in olivine and implications for properties of the shallow mantle. Earth Planet Sci Lett 403: 37–47

Zhao Y-H, Ginsberg SB, Kohlstedt DL (2004) Solubility of hydrogen in olivine: dependence on temperature and iron content. Contrib Mineral Petrol 147: 155–161